HAL
open science

Microstructure and mechanical properties relationship of additively manufactured 316L stainless steel by selective laser melting

Anne-Helene Puichaud, Camille Flament, Aziz Chniouel, Fernando Lomello, Elodie Rouesne, Pierre-François Giroux, Hicham Maskrot, Frederic Schuster, Jean-Luc Béchade

To cite this version:

Anne-Helene Puichaud, Camille Flament, Aziz Chniouel, Fernando Lomello, Elodie Rouesne, et al.. Microstructure and mechanical properties relationship of additively manufactured 316L stainless steel by selective laser melting. EPJ N - Nuclear Sciences & Technologies, 2019, 5, pp.23. 10.1051/epjn/2019051 . cea-02458434

HAL Id: cea-02458434

https://cea.hal.science/cea-02458434v1

Submitted on 29 Jan 2020

HAL is a multi-disciplinary open access archive for the deposit and dissemination of scientific research documents, whether they are published or not. The documents may come from teaching and research institutions in France or abroad, or from public or private research centers.

L'archive ouverte pluridisciplinaire **HAL**, est destinée au dépôt et à la diffusion de documents scientifiques de niveau recherche, publiés ou non, émanant des établissements d'enseignement et de recherche français ou étrangers, des laboratoires publics ou privés.

EPJ Nuclear Sci. Technol. **5**, 23 (2019)
© A.-H. Puichaud et al., published by EDP Sciences, 2019
https://doi.org/10.1051/epjn/2019051

EPJ Nuclear Sciences & Technologies

Available online at:
https://www.epj-n.org

Regular Article

Open Access

Microstructure and mechanical properties relationship of additively manufactured 316L stainless steel by selective laser melting

Anne-Helene Puichaud[1,*], Camille Flament[1], Aziz Chniouel[2], Fernando Lomello[2], Elodie Rouesne[3], Pierre-François Giroux[3], Hicham Maskrot[2], Frederic Schuster[4], and Jean-Luc Béchade[1]

[1] DEN – Service de Recherches en Métallurgie Physique, CEA, Université Paris-Saclay, 91191 Gif-sur-Yvette, France
[2] DEN – Service d'Etudes Analytiques et de Réactivité des Surfaces, CEA, Université Paris-Saclay, 91191 Gif-sur-Yvette, France
[3] DEN – Service de Recherches Métallurgiques Appliquées, CEA, Université Paris-Saclay, 91191 Gif-sur-Yvette, France
[4] Cross-Cutting Skills Program on Materials and Processes, CEA, Université Paris-Saclay, 91191 Gif-sur-Yvette, France

Received: 24 January 2019 / Received in final form: 24 September 2019 / Accepted: 23 October 2019

Abstract. Additive manufacturing (AM) is rapidly expanding in many industrial applications because of the versatile possibilities of fast and complex fabrication of added value products. This manufacturing process would significantly reduce manufacturing time and development cost for nuclear components. However, the process leads to materials with complex microstructures, and their structural stability for nuclear application is still uncertain. This study focuses on 316L stainless steel fabricated by selective laser melting (SLM) in the context of nuclear application, and compares with a cold-rolled solution annealed 316L sample. The effect of heat treatment (HT) and hot isostatic pressing (HIP) on the microstructure and mechanical properties is discussed. It was found that after HT, the material microstructure remains mostly unchanged, while the HIP treatment removes the materials porosity, and partially re-crystallises the microstructure. Finally, the tensile tests showed excellent results, satisfying RCC-MR code requirements for all AM materials.

1 Introduction

Additive manufacturing (AM) is being extensively developed as a promising technology and is already exploited in various industries, in particular in biomedical and aerospace applications [1,2].

AM process has key industrial advantages such as the ability to create complex geometries, to repair existing parts, and rapid prototyping. Such advantages could be exploited for nuclear industries, but little work has been done to date in this field [3,4]. However AM technologies lead to complex materials microstructure, anisotropy and residual porosity.

Austenitic stainless steel (SS) is extensively used in the internal structure of generation III reactors and promising candidate for generation IV reactors due to their excellent corrosion resistance and good mechanical properties at service temperature and pressure. Therefore, the stability of the microstructure under irradiation, i.e. the austenitic phase, is crucial to ensure the corrosion resistance durability for nuclear applications. A homogeneous distribution of the elements in solid solution, while avoiding localised Cr depletion that would make the SS sensitive to corrosion is also essential. One of the key microstructural evolutions of materials under irradiation, specifically 316L-type austenitic stainless steel, is the swelling, the stress-free change of dimensions of the material due to the formation of voids, bubbles or even phase transformation. Therefore, the non-irradiated material is initially required to be as dense as possible to limit swelling.

Previous research has shown that selective laser melting (SLM) additive manufacturing creates very complex microstructures with usually anisotropic grain morphologies [5], a high density of dislocations, porosity and heterogeneous distribution of solutes in the materials. The presence of sub-grains has been shown by others in SLM fabricated 316L SS [6,7] and in Ni-based superalloys [8] and that the sub-grain boundaries are entangled dislocation lines.

SLM machine processing parameters influence the microstructure of the final material. Most 316L SLM fabricated materials exhibit melt pools [9–13], and an

* e-mail: anne-helene.puichaud@cea.fr

This is an Open Access article distributed under the terms of the Creative Commons Attribution License (https://creativecommons.org/licenses/by/4.0), which permits unrestricted use, distribution, and reproduction in any medium, provided the original work is properly cited.

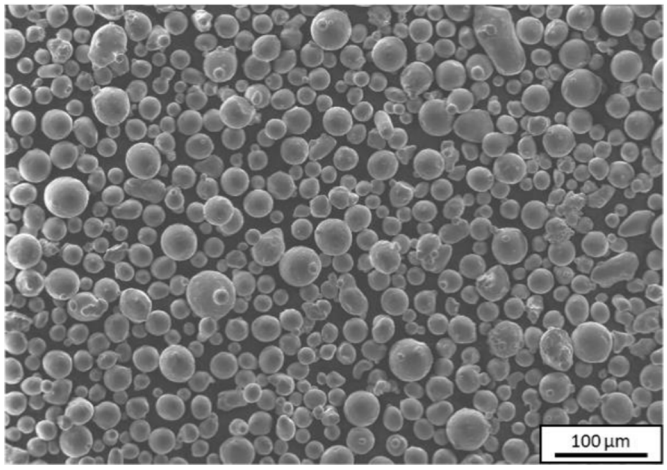

Fig. 1. SEM micrograph of the raw 316L SS powder showing the spherical beads.

anisotropic microstructure with elongated grains in the fabrication direction [5,14,15]. Precipitates have previously been observed in as-built 316L SLM fabricated stainless steels. The chemical composition of those nanoparticles is different from one study to another [6,7]. Post-fabrication thermal treatments can be used to compensate materials morphologies that are inherent to AM process [16,7]. Those microstructural differences ultimately influence mechanical properties such as resilience behaviour [17–20,16,13].

In this study, 316L-type austenitic stainless steel cubes were fabricated by SLM using commercial 316L powder, with AM fabricated materials studied as-built, after a stress-relieved heat treatment (HT) and after a hot isostatic pressing (HIP). The aim of this study is to determine the influence of heat treatment and hot isostatic pressure on the microstructure and mechanical properties of AM fabricated 316L SS, for potential nuclear applications. To this end, an in-depth microstructural characterisation of the as-built, HT and HIP materials have been performed. Tensile tests were used to determine the impact of these different microstructures on mechanical properties. The AM fabricated materials microstructure and mechanical tests results are compared to a reference material, a 316L stainless steel, initially cold-rolled then solution annealed (SA) and followed by a quenching.

2 Experimental procedure

2.1 Raw material

Argon-atomised spherical 316L SS powder supplied by Trumpf GmbH was used. The powder is characterised by spherical beads with only a small amount of satellites and rod-like particles as shown in Figure 1. Particle size measured by Partica using the Fraunhofer laser diffraction method vary from 20 to 40 μm and the size distribution values D10, D50 and D90 are 20.6; 28.3 and 39.5, respectively. The apparent density measured according to the standard ASTM B212 is $4.39 \pm 0.01\,\mathrm{g/cm^3}$. Moreover, flow properties, determined by Densitap device provided by GranuloShop revealed a Carr index of 7% and a Hausner index of 1.043, both showing the good flow-behaviour of the powder [21,22]. Major elements were quantified by inductively coupled plasma optical emission spectrometry (ICP-OES), minor elements by GDMS and gas elements by instrumental gas analysis (IGA) EMGA-820 analyser.

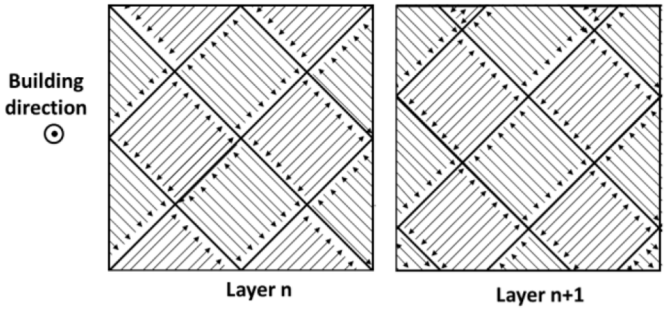

Fig. 2. Schematic of the laser scanning strategy for two consecutive layers (n and n+1) showing the 90° rotation between each island.

2.2 Process parameters

The samples were manufactured using a Trumpf TruPrint Series 1000 3D printer, equipped with an Yb fibre laser (wavelength $\lambda = 1064$ nm) and a Gaussian beam spot of 55 μm diameter. The scanning was performed using a laser power of 150 W with a speed of 675 mm/s. A layer of powder of 20 μm thickness and a hatching distance of 90 μm were applied. Processing was conducted in Ar atmosphere to avoid oxidation and impurity contamination. Residual oxygen in the build chamber was fixed at <100 ppm. The set scanning strategy was 4 mm^2 islands with a rotation of 90° between each island (Fig. 2).

For microstructural and chemical analysis, cubes of $1\times1\times1.5\,\mathrm{cm}^3$ were manufactured and samples were prepared appropriately for each characterisation technique. After AM fabrication, two separate post-treatment conditions were carried out on as-built samples in order to assess the impact of post treatments on microstructure and mechanical properties. The first one was a heat treatment (HT) in Ar atmosphere up to 700 °C and held for 1 h. The second one was a hot isostatic pressure (HIP) treatment, heated to 1100 °C and held for 3 h at a pressure of 1800 bar in Ar atmosphere. Both heat treatments had a heating and a cooling ramp of approximately 800 °C/h.

2.3 Microstructural characterisations

2.3.1 XRD

X-ray diffraction (XRD) measurements were conducted using a Brücker D8 Advance diffractometer with a Bragg–Brentano θ-2θ geometry and a Cu K_α radiation source.

2.3.2 OM

Optical microscopy (OM) imaging was carried out with a Reichert-Jung MeF3 on samples that were mechanically polished, then electropolished in 10 vol.% oxalic acid to reveal melt pools and grain boundaries.

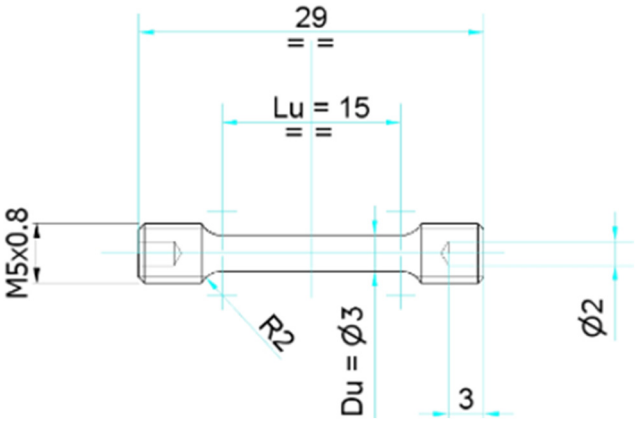

Fig. 3. Schematic of a sample dimension for tensile tests (units in mm).

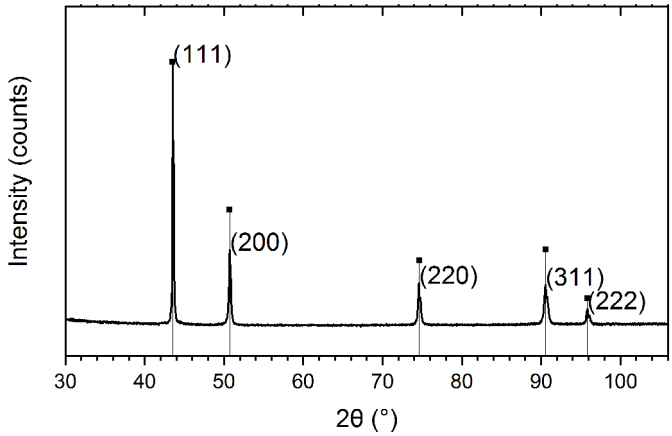

Fig. 4. XRD θ-2θ scan of the 316L SS Trumpf powder showing the first five (hkl) peaks of the pure austenitic phase (■) [24].

Table 1. Chemical composition of the 316L raw powder and of the SA plate (in wt.%) alongside the RCC-MR code requirements.

	Cr	Ni	Mn	Si	Mo	C	N	O	S	P	Fe
RCC-MR code	16.5–18.5	10–13	≤2	≤1	2–2.5	≤0.03	≤0.110	–	≤0.015	≤0.030	Bal.
Trumpf 316L powder	17.55	11.75	1.15	0.45	2	0.018	0.0877	0.0975	0.0065	≤0.001	Bal.
316L SA	17.44	12.33	1.82	0.46	2.3	0.024	0.060	–	0.001	0.027	Bal.

2.3.3 EBSD analysis

Electron backscattered diffraction (EBSD) analysis was performed to determine the grain morphology and grain orientation of the samples. The EBSD characterisations were carried out on a Zeiss Sigma HD scanning electron microscope (SEM) operated at 20 kV. The EBSD data acquisition was performed using a Bruker e-Flash HR detector, and was processed by Esprit Bruker software packages. The step size was 0.47 μm. The average grain size measurements were performed with a grain tolerance angle of 10°. The twin boundaries were defined as coincident site lattice boundaries for 60° rotation on the ⟨111⟩ direction. The mechanically polished samples were electropolished using a perchloric acid solution to remove irregularities and any deformation layer from the surface.

2.3.4 TEM specimen preparation

Slices of the materials were mechanically thinned to approximately 100 μm using SiC grinding discs and 1 μm diamond paste finish. 3-mm discs were punched from these slices and thinned to electron transparency using a Tenupol-5 twin-jet electropolisher. The voltage for jet-polishing was set between 20 and 25 V, the electrolyte was a solution of 10 vol.% perchloric acid and 20 vol.% ether 2-butoxyethanol in ethanol and the temperature was maintained to 5 °C.

2.3.5 TEM

Microstructural examinations were performed using a Thermo Fischer Scientific Tecnai G20 transmission electron microscope (TEM) equipped with a LaB_6 filament operated at 200 keV and a charged coupled device camera for images and diffraction patterns acquisition. Energy dispersive spectroscopy (EDS) was also conducted in the TEM for chemical analysis using a synergie[4]/Bruker Silicon drift EDS detector. STEM images were recorded using high angular annular dark field (HAADF) and bright field (BF) detectors and a low camera length was used to minimise the diffraction contrast. The statistical analysis of the materials porosity was determined by image analysis using Thermo Fischer Scientific Visilog Software.

2.4 Mechanical characterisations: tensile tests

Five cylindrical ($\varphi = 8 \times 35$ mm^2) beam-like samples were manufactured along the build direction (BD) (parallel to the Z-axis) and machined to shape for tensile tests (Fig. 3). Specimens were tested with a strain rate of 10^{-3} s^{-1} at room temperature.

3 Results

The as-received Trumpf powder and the reference SA materials chemical composition is listed in Table 1 and both compositions meet the RCC-MR code requirements for 316L used in nuclear field [23]. XRD results (Fig. 4) confirm a fully γ-austenite 316L SS powder with a face-centred cubic structure with a lattice parameter of 3.596 ± 0.001 Å.

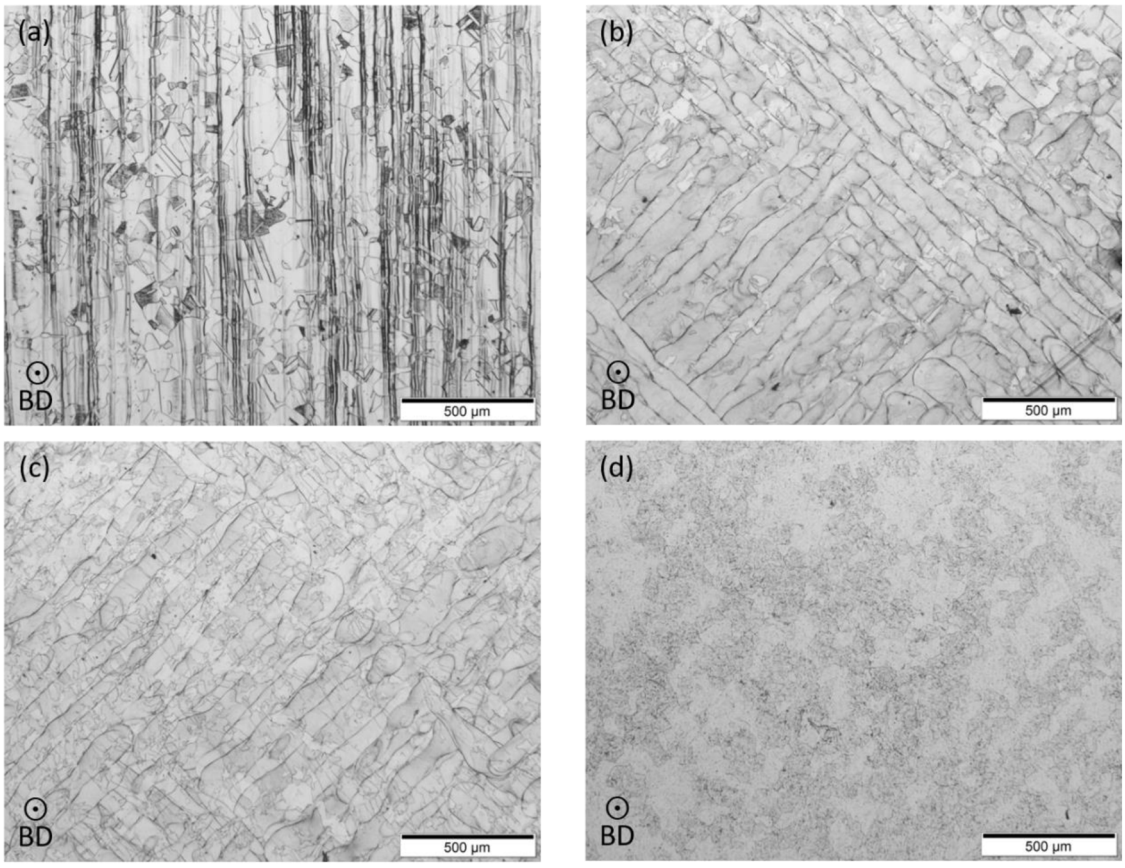

Fig. 5. OM images of 316L materials in the fabrication plane: (a) SA, (b) AM as-built, (c) AM HT and (d) AM HIP. Build direction (BD) out-of-plane.

3.1 Microstructure

3.1.1 Grain morphology and orientation

The OM images presented in Figure 5 show the microstructure of the three AM materials, compared to the SA reference. The SA sample exhibits a crystalline microstructure and presents ferrite planes along the lamination direction as expected in those materials. The chemical etching of the as-built and HT AM samples clearly revealed the melt pools characteristic of the SLM technique. After HIP treatment, the melt pools completely disappeared.

The grain orientation and the grain size were determined using EBSD-SEM. Figure 6 shows EBSD orientation maps by the Inverse Pole Figures (IPF) with the ⟨uvw⟩ directions parallel to the BD, with corresponding pole figures.

The reference 316L SA plate material presents no preferred crystallographic orientation, as shown by the IPF maps and the pole figures in Figures 6a and 6b. The average grain size was measured to be approximately 40 μm, with little elongation in the lamination direction (Tab. 2). The phase is nearly fully γ-austenitic and approximately 1–2% δ-ferrite was detected. Almost all the grains present twin boundaries in the SA 316L sample.

As expected, the AM as-built sample exhibits a strong epitaxial orientation in the ⟨110⟩ direction along the BD, presenting a near α-fibre crystallographic orientation, with elongated columnar grains across several melt pools. A {110}⟨001⟩ Goss texture along the laser scanning direction (SD) is also observed (Fig. 6c).

The HT sample still exhibits a preferential {110}⟨001⟩ Goss texture along the SD, with a less pronounced ⟨110⟩ fibre texture as shown in Figure 6e with more (⟨100⟩// BD) columnar grains than AM fabricated as-built sample (Fig. 6c).

EBSD analysis also revealed that all of the as-built and HT samples grains present a strong intra-granular misorientation and none are twin boundaries. No grain boundaries closed in finite grains in both the XY plane and Z direction could be defined. Consequently the grain size was not determined for the as-built and the HT samples.

On the other hand, the microstructure of the HIP sample is bimodal, characterised by two populations of grains in terms of morphology, microstructural state and local crystallographic texture (Figs. 6g, 6h). Approximately half of the grains remain columnar grains elongated and orientated in the ⟨110⟩ direction along the BD and the other half of the grains are twinned, re-crystallised and randomly oriented. The columnar grains still present intra-granular misorientation inherited from the as-built state. The grain size was measured at approximately 45 μm. This shows that the HIP AM material presents grains closer to the SA microstructure in terms of shape, size and crystallisation. Finally, no ferrite was detected in any of the AM fabricated samples with EBSD analysis.

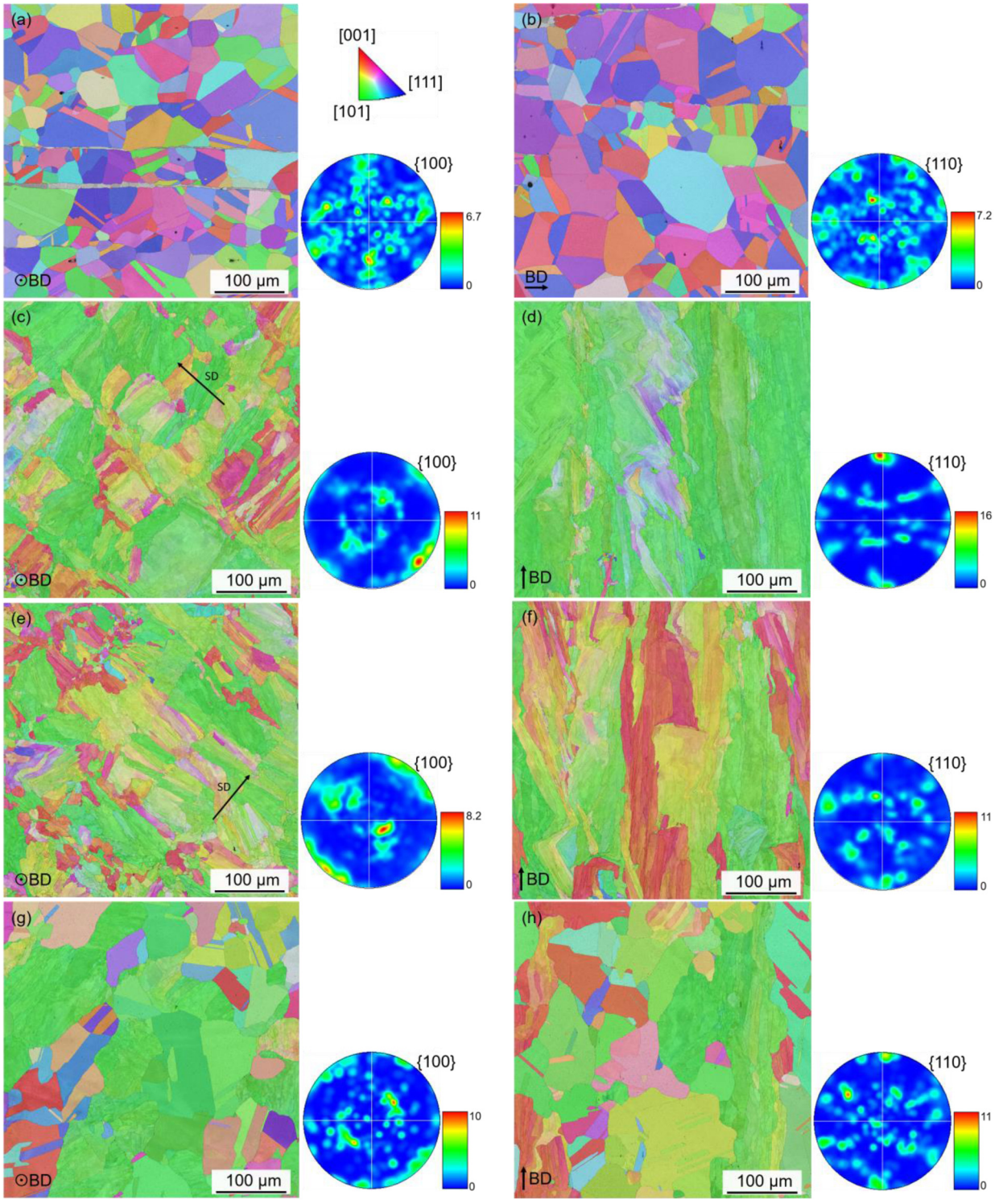

Fig. 6. EBSD inverse pole figure (IPF) maps with corresponding pole figures of the 316L materials: (a,b) SA, (c, d) AM as-built, (e, f) AM HT and (g, h) AM HIP. For (a, c, e, g), the specimens were cut normal to the build direction (BD), and for (b, d, f, h) they were cut along the BD. The IPF colour scale is in (a).

3.1.2 Dislocations

TEM images in Figure 7 show a detailed microstructure of the AM materials. Here the columnar dendritic cell structure within the grains are clearly visible and elongated in the build direction in the as-built (Fig. 7a) and the HT samples (Fig. 7b). The cells are defined by a high density of tangled dislocations. The presence of the dislocations is consistent with the strong intra-granular misorientation found in EBSD analysis. Figure 7c shows the grain boundary (GB)

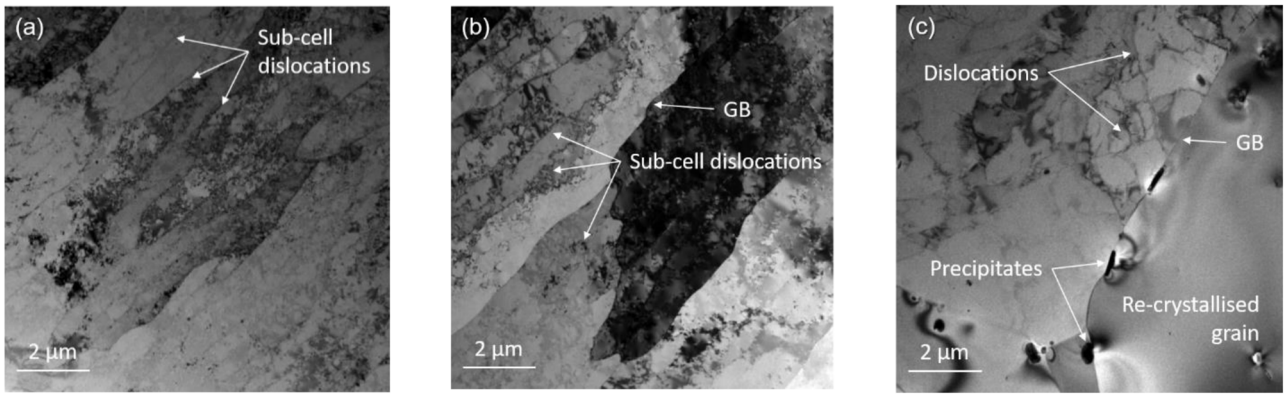

Fig. 7. Conventional TEM micrographs of the 316L AM materials: (a) as-built, (b) heat-treated and (c) HIP, showing GB and the sub-grain structure in the as-built and HT samples. The three specimen were prepared in a plane along the build direction. The HIP sample presents precipitates at GB and re-crystallised structure with residual dislocations.

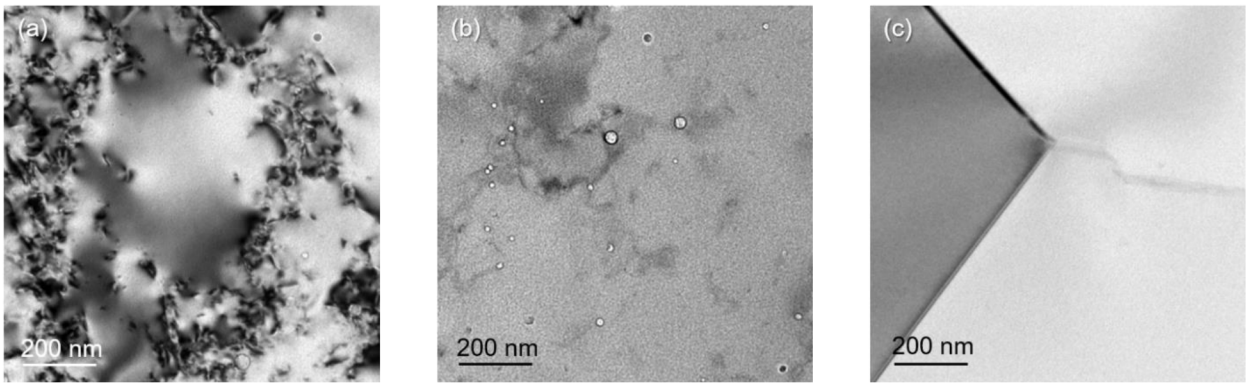

Fig. 8. Conventional TEM micrographs of the 316L AM materials showing the tangled dislocation of a dendritic cell in the as-built (a), the nanoporosity in the HT sample (b) and a grain boundary free of porosity in the HIP sample (c).

Table 2. Average grain size of the samples in the XY plane and along the build direction (Z) measured using EBSD.

	Average grain size (μm)	
	XY	Z
SA	35	45
As-built AM	Not defined	Not defined
HT AM	Not defined	Not defined
HIP AM	48	41

between a grain with a high density of dislocations and a re-crystallised grain in which the dendritic cells have disappeared after HIP treatment, again matching the EBSD results with low intra-granular misorientation.

3.1.3 Porosity

The densities measured using Archimedes' principle method revealed that all the AM materials present a density higher than 99.9% and no significant variation is detected after HT. This result was previously showed by Röttger et al. [25] for shorter HIP treatment up to 1050 °C on SLM materials. However, our TEM image analysis reveals the presence of nanoporosity in the as-built and the HT samples (Fig. 8). Although it is homogenously distributed in the sample, the TEM image in Figure 8b shows that this nanoporosity is usually near dislocations. The apparent diameter ranges between 5 and 60 nm in both samples. Figure 9 shows that the heat treatment has little influence on the nanoporosity size present in the AM material, even though its density slightly increases (Tab. 3). This nanoporosity however disappears after HIP treatment (Fig. 8c).

3.1.4 Precipitation and segregation

EDS results show that the as-built AM sample presents segregation of Mo which is located at the cell boundaries (Fig. 10). This result is consistent with results found by other authors [6]. Amorphous precipitation of (Mn, Si) oxides was found homogeneously dispersed in the samples (Fig. 10). These precipitates crystallise after the HT at 700 °C, but their size and density in the material remained unchanged (Tab. 3). In contrast, the HIP sample presents much larger precipitates as illustrated in (Fig. 7c).

Table 3. Average diameter and density of the pores and precipitates observed in the AM fabricated 316L SS.

	Pores		Precipitates	
	d (nm)	ρ ($10^{18}/m^3$)	d (nm)	ρ ($10^{18}/m^3$)
As-built AM	24 ± 1	74	47 ± 2	35
HT AM	29 ± 1	119	42 ± 2	54
HIP AM	–	–	453 ± 35	1

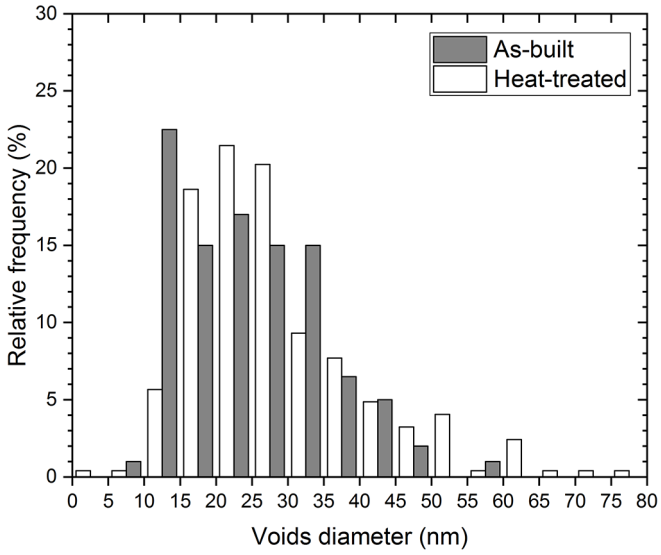

Fig. 9. Relative frequency of the nanoporosity diameter measured in the as-built and the HT AM 316L SS.

TEM-EDS analysis confirmed that the precipitates in the AM HIP sample are Mn-Si oxides (Fig. 11). The precipitates exhibit a stick shape with width of a few hundred nanometres and a length ranging between 80 and 4000 nm, and 95% have a length lower than 1 μm. This precipitation is believed to originate from the growth of the (Mn, Si) oxides already present in the as-built samples. No Mo segregation is observed at grain boundaries, nor near the remaining dislocations in the HIP sample.

3.2 Tensile tests

Figure 12a shows typical tensile test curves measured on AM fabricated materials and the average tensile strength results are presented in Figure 12b. The yield strength (YS) of the as-built AM material (520 ± 7 MPa) is higher than the one of the HT (430 ± 2 MPa) and the HIP (271 ± 2 MPa) materials. The ultimate tensile strength (UTS) on the other hand show little variation with the post fabrication treatments (576 ± 2 MPa and 570 ± 1 MPa for the HT and the HIP materials, respectively) even though the as-built sample presents a slightly higher value (584 ± 3 MPa). The materials also showed excellent elongation at fracture results (77%, 73% and 80% for the as-built, HT and HIP materials, respectively). All the AM samples meet the RCC-MR code requirements for nuclear applications in terms of YS, UTS and elongation at fracture.

4 Discussions

4.1 Microstructures

For nuclear applications, in particular for future sodium-cooled fast reactors, the structural material of choice in the reactor is 316L-type stainless steel for its excellent corrosion resistance and mechanical properties [26]. The downside of 316L-type materials however is their swelling under irradiation favoured by their face centred cubic structure. Dislocations play a role in the swelling process as they act as defect sinks [27]. Therefore, void-swelling should be reduced in presence of a high density of dislocation lines. However, the materials present a very complex microstructure and the effect of each defect on swelling may not be quantified and interpreted independently from one another. The small intragranular cells, alongside the high density of dislocations in the HT materials, would potentially be an advantage to lower swelling under irradiation, as the dislocations act as vacancy sinks. However, the nanoporosities present in those materials would act as sinks and be in favour to void and cavity growth, potentially furthering the swelling under irradiation. The HIP treatment however allowed a full densification with the loss of the nanoporosity that was observed in the as-built and the HT samples. Half of the grains were re-crystallised, lowering the density of dislocations without completely removing them. Therefore, considering only the microstructure of the materials, it would be expected that the combination of a lower dislocation density and the absence of porosity would make the HIP AM sample the material of choice under irradiation. However, the presence of precipitates could potentially be detrimental due to cavity creation, under irradiation, at their interface with the matrix

4.2 Tensile tests

The YS significantly decreases with the HT and the HIP. The higher YS value of the as-built AM sample is explained by the smaller grains and the high intragranular misorientation of the as-built material compared to the HT and the HIP samples. On the other hand, the HT and HIP treatments have no effect on the UTS. This shows that the [110] preferential orientation along the build direction has no effect on the material hardness. For the YS and the UTS results, it is worth noting that the results between tests for each metallurgical state were reasonably similar as shown by the low interval of confidence of the average results. In contrast, the elongation at fracture presents more scattered

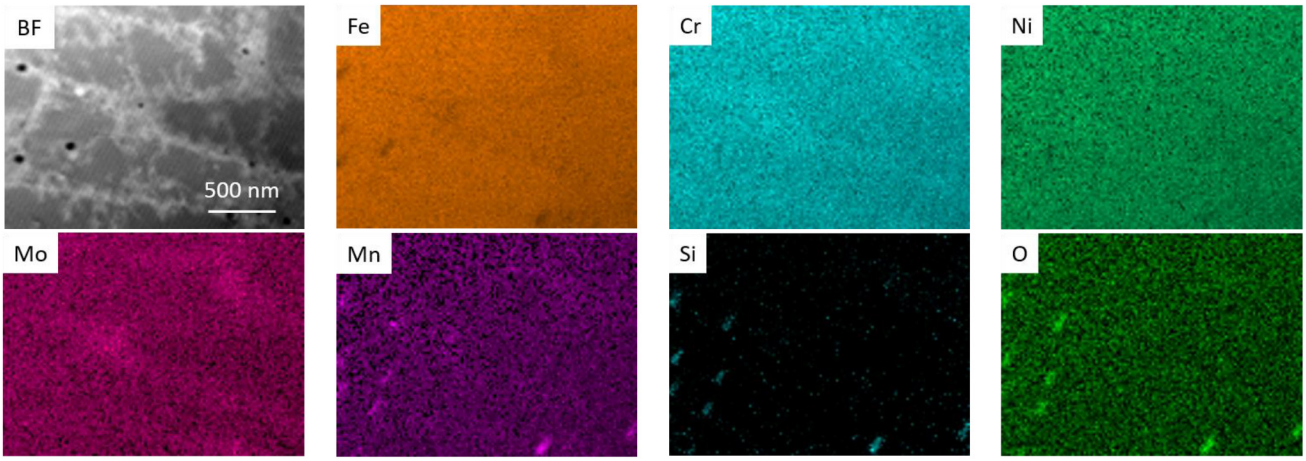

Fig. 10. STEM bright field (BF) image of the AM as-built sample and EDS elemental maps of Fe, Cr, Ni, Mn, Si, Mo and O. Scale in BF image.

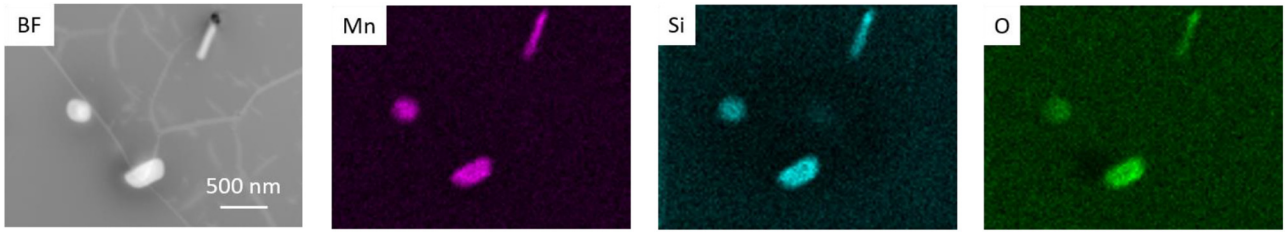

Fig. 11. STEM bright field (BF) image of the AM HIP sample and EDS elemental maps of Mn, Si, and O. Scale in BF image.

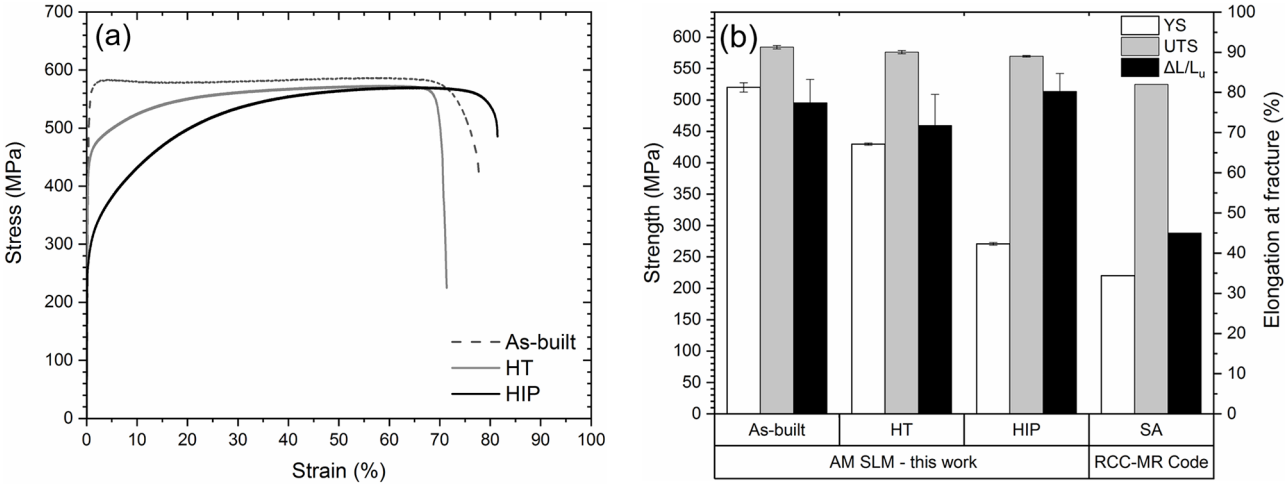

Fig. 12. Tensile tests of the AM as-built, HT and HIP materials. (a) Representative stress versus strain curves. (b) Tensile tests measured on 5 tests samples of the AM fabricated materials, compared to the maximal values allowed by the RCC-MR code for a CW 316L SS. Left axis: yield strength (YS) and ultimate tensile strength (UTS), and right axis: elongation at fracture ($\Delta L/L_u$).

results thus a larger interval of confidence relative to the average, as is often found for elongation results [13,25,28]. The elongation at fracture is therefore considered somewhat comparable for the three AM materials. The elongation values for all three AM materials are significantly higher than most of those found in literature, with values ranging from 10 to 50% for SLM 316L as-built materials [13,19,29–31], 25–55% for those with a post-fabrication HT between 600 and 1100 °C [6,28,30] and 38–41% for HIP treated ones [16,25]. A few studies reported similar values of elongation at fracture (around 80%) [32,33] for as-built and HIP samples. It must also be noted

that tensile tests results, especially elongation at fracture, are sample geometry and test parameters dependant. Nonetheless, the YS and UTS values results in this study fall in the range of values found in the literature with or without post fabrication treatment. Finally, French authorities have implemented high standards and codes for nuclear components [34]. The tensile tests meet the RCC-MR code requirements for nuclear applications in terms of YS, UTS and elongation at fracture. This is an indispensable condition for materials to be considered for use in nuclear applications.

5 Conclusions

This study showed that the SLM process and the HT and HIP treatment lead to complex microstructures. The grains in the as-built samples present a [110] preferential orientation along the build direction (near α-fibre texture), which eases with heat treatment and nearly disappears with HIP. All AM materials present a high density (>99.9 %), however nanoporosity was identified in the as-built and HT samples, and it disappeared after HIP treatment. Amorphous precipitates of Mn and Si oxides were observed in the as-built AM sample. These precipitates crystallised with HT treatment without growth, and the HIP treatment led to the growth of the precipitates.

This study, placed in the context of nuclear applications, showed that before irradiation the AM materials exhibit suitable yield strength, ultimate tensile strength and elongation in the non-irradiated tested conditions, satisfying the RCC-MR code requirements. The recrystallisation of 50% of the grains alongside the disappearance of the dendritic cells by the HIP treatment likely led to the decrease of the yield strength values, but this was to the advantage of a higher YS/UTS ratio. The different microstructures of those materials would likely present different responses to irradiation, and in particular in terms of swelling. The high density and void-free HIP AM material is possibly the best candidate for nuclear application with regard to swelling response and would require further study.

The authors would like to thank Dr. J. Malaplate and Dr. A. Renault-Laborne for valuable discussions, B. Arnal for creating macros necessary for particle analysis in Visilog Xpert 7.2 image processing software. This study was funded by Cross-Cutting Skills Program on Materials and Processes (CEA).

Author contribution statement

A.-H.P. and C.F. performed TEM and EDS characterisation and wrote the manuscript. A.Z. fabricated the materials and performed mechanical testing together with P.-F.G. EBSD characterisation was made by E.R. J.-L.B. supervised the project. The results were discussed with all the co-authors.

References

1. S.S. Leong, A. Jia, Y.W. Yee, W.F. Edith, Laser and electron-beam powder-bed additive manufacturing of metallic implants: A review on processes, materials and designs, J. Orthop. Res. **34**, 369 (2015)
2. S. Singh, S. Ramakrishna, R. Singh, Material issues in additive manufacturing: A review, J. Manuf. Process. **25**, 185 (2017)
3. X. Lou, M. Song, P.W. Emigh, M.A. Othon, P.L. Andresen, On the stress corrosion crack growth behaviour in high temperature water of 316L stainless steel made by laser powder bed fusion additive manufacturing, Corros. Sci. **128**, 140 (2017)
4. X. Lou, P.L. Andresen, R.B. Rebak, Oxide inclusions in laser additive manufactured stainless steel and their effects on impact toughness and stress corrosion cracking behavior, J. Nucl. Mater. **499**, 182 (2018)
5. T. Niendorf, S. Leuders, A. Riemer, H.A. Richard, T. Tröster, D. Schwarze, Highly anisotropic steel processed by selective laser melting, Metall. Mater. Trans. B **44**, 794 (2013)
6. K. Saeidi, X. Gao, Y. Zhong, Z.J. Shen, Hardened austenite steel with columnar sub-grain structure formed by laser melting, Mater. Sci. Eng. A **625**, 221 (2015)
7. D. Kong, X. Ni, C. Dong, L. Zhang, C. Man, J. Yao, K. Xiao, X. Li, Heat treatment effect on the microstructure and corrosion behavior of 316L stainless steel fabricated by selective laser melting for proton exchange membrane fuel cells, Electrochim. Acta **276**, 293 (2018)
8. T. Vilaro, C. Colin, J.D. Bartout, L. Nazé, M. Sennour, Microstructural and mechanical approaches of the selective laser melting process applied to a nickel-base superalloy, Mater. Sci. Eng. A **534**, 446 (2012)
9. M. Zietala, T. Durejko, M. Polanski, I. Kunce, T. Płocinski, W. Zielinski, M. azinska, W. Stepniowski, T. Czujko, K.J. Kurzydłowski, Z. Bojar, The microstructure, mechanical properties and corrosion resistance of 316L stainless steel fabricated using laser engineered net shaping, Mater. Sci. Eng. A **677**, 1 (2016)
10. E. Liverani, S. Toschi, L. Ceschini, A. Fortunato, Effect of selective laser melting (SLM) process parameters on microstructure and mechanical properties of 316L austenitic stainless steel, J. Mater. Process. Technol. **249**, 255 (2017)
11. A. Leicht, U. Klement, E. Hryha, Effect of build geometry on the microstructural development of 316L parts produced by additive manufacturing, Mater. Charact. **143**, 137 (2018)
12. P. Köhnen, C. Haase, J. Bültmann, S. Ziegler, J.H. Schleifenbaum, W. Bleck, Mechanical properties and deformation behavior of additively manufactured lattice structures of stainless steel, Mater. Des. **145**, 205 (2018)
13. T. Kurzynowski, K. Gruber, W. Stopyra, B. Kuznicka, E. Chlebus, Correlation between process parameters, microstructure and properties of 316L stainless steel processed by selective laser melting, Mater. Sci. Eng. A **718**, 64 (2018)
14. D. Tomus, Y. Tian, P.A. Rometsch, M. Heilmaier, X. Wu, Influence of post heat treatments on anisotropy of mechanical behaviour and microstructure of Hastelloy-X parts produced by selective laser melting, Mater. Sci. Eng. A **667**, 42 (2016)

15. Z. Wang, T.A. Palmer, A.M. Beese, Effect of processing parameters on microstructure and tensile properties of austenitic stainless steel 304L made by directed energy deposition additive manufacturing, Acta Mater. **110**, 226 (2016)
16. N.P. Lavery, J. Cherry, S. Mehmood, H. Davies, B. Girling, E. Sackett, S.G.R. Brown, J. Sienz, Effects of hot isostatic pressing on the elastic modulus and tensile properties of 316L parts made by powder bed laser fusion, Mater. Sci. Eng. A **693**, 186 (2017)
17. A. Riemer, S. Leuders, M. Thöne, H.A. Richard, T. Tröster, T. Niendorf, On the fatigue crack growth behavior in 316L stainless steel manufactured by selective laser melting, Eng. Fract. Mech. **120**, 15 (2014)
18. J.A. Cherry, H.M. Davies, S. Mehmood, N.P. Lavery, S.G.R. Brown, J. Sienz, Investigation into the effect of process parameters on microstructural and physical properties of 316L stainless steel parts by selective laser melting, Int. J. Adv. Manuf. Technol. **76**, 869 (2015)
19. A.A. Deev, P.A. Kuznetcov, S.N. Petrov, Anisotropy of mechanical properties and its correlation with the structure of the stainless steel 316L produced by the SLM method, Phys. Procedia **83**, 789 (2016)
20. R. Casati, J. Lemke, M. Vedani, Microstructure and fracture behavior of 316L austenitic stainless steel produced by selective laser melting, J. Mater. Sci. Technol. **32**, 738 (2016)
21. R.L. Carr, Evaluating flow properties of solids, Chem. Eng. **72**, 163 (1965)
22. D. McGlinchey, *Bulk solids handling: equipment selection and operation*, 1st edn. (Blackwell Publising, New Jersey, 2008)
23. Design and Construction Rules for Mechanical Components of the FBR Nuclear Installations, 2007
24. D. Pfoertsch, C. Ruud, Penn State University, ICDD Grant-in-Aid, PDF 33-0397, 1983
25. A. Röttger, K. Geenen, M. Windmann, F. Binner, W. Theisen, Comparison of microstructure and mechanical properties of 316L austenitic steel processed by selective laser melting with hot-isostatic pressed and cast material, Mater. Sci. Eng. A **678**, 365 (2016)
26. CEA, La technologie des RNR-Na, in: Réact. Nucl. À Caloporteur Sodium, Le Moniteur, 2014, p. 276
27. G. Was, *Fundamentals of radiation materials science: metals and alloys* (Springer, Berlin, 2017)
28. H.D. Carlton, A. Haboub, G.F. Gallegos, D.Y. Parkinson, A. A. MacDowell, Damage evolution and failure mechanisms in additively manufactured stainless steel, Mater. Sci. Eng. A **651**, 406 (2016)
29. W. Shifeng, L. Shuai, W. Qingsong, C. Yan, Z. Sheng, S. Yusheng, Effect of molten pool boundaries on the mechanical properties of selective laser melting parts, J. Mater. Process. Technol. **214**, 2660 (2014)
30. M. Montero Sistiaga, S. Nardone, C. Hautfenne, J. Van Humbeeck, Effect of heat treatment of 316L stainless steel produced by selective laser melting (SLM), in *Proceedings of the 27th Annual International Solid Freeform Fabrication Symposium – An Additive Manufacturing Conference, 2016*, pp. 558–565, available at https://lirias.kuleuven.be/handle/123456789/548789 (accessed December 21, 2017)
31. J. Suryawanshi, K.G. Prashanth, U. Ramamurty, Mechanical behavior of selective laser melted 316L stainless steel, Mater. Sci. Eng. A **696**, 113 (2017)
32. R.M. Horn, M. Connor, D. Webber, J. Jackson, F. Bolger, Evaluation of additively manufactured materials for nuclear plant components, in: J.H. Jackson, D. Paraventi, M. Wright (Eds.), in *Proceedings of the 18th International Conference on Environmental Degradation of Materials in Nuclear Power Systems – Water Reactor* (Springer International Publishing, Berlin 2018), pp. 1009–1020
33. Y.M. Wang, T. Voisin, J.T. McKeown, J. Ye, N.P. Calta, Z. Li, Z. Zeng, Y. Zhang, W. Chen, T.T. Roehling, R.T. Ott, M.K. Santala, P.J. Depond, M.J. Matthews, A.V. Hamza, T. Zhu, Additively manufactured hierarchical stainless steels with high strength and ductility, Nat. Mater. **17**, 63 (2018)
34. R. Noel, The new code "RCC-MR" – Rules for design and construction of LMFBR components, Nucl. Eng. Des. **98**, 297 (1987)

Cite this article as: Anne-Helene Puichaud, Camille Flament, Aziz Chniouel, Fernando Lomello, Elodie Rouesne, Pierre-François Giroux, Hicham Maskrot, Frederic Schuster, Jean-Luc Béchade, Microstructure and mechanical properties relationship of additively manufactured 316L stainless steel by selective laser melting, EPJ Nuclear Sci. Technol. **5**, 23 (2019)